The Role of Particles in the Inhibition of Counterflow Diffusion Flames by Iron Pentacarbonyl☆

MARC D. RUMMINGER,† and GREGORY T. LINTERIS*

Building and Fire Research Laboratory, National Institute of Standards and Technology, Gaithersburg, MD 20899, USA

Laser light scattering and thermophoretic sampling have been used to investigate particle formation in counterflow diffusion flames inhibited by iron pentacarbonyl $Fe(CO)_5$. Three CH_4-O_2-N_2 reactant mixtures are investigated, with $Fe(CO)_5$ added to the fuel or the oxidizer stream in each. Flame calculations that incorporate only gas-phase chemistry are used to assist in interpretation of the experimental results. In flames with the inhibitor added on the flame side of the stagnation plane, the region of particle formation overlaps with the region of high H-atom concentration, and particle formation may interfere with the inhibition chemistry. When the inhibitor is added on the non-flame side of the stagnation plane, significant condensation of metal or metal oxide particles is found, and implies that particles prevent active inhibiting species from reaching the region of high radical concentration. As the inhibitor loading increases, the maximum scattering cross section increases sharply, and the difference between the measured and predicted inhibition effect widens, suggesting that particle formation is the cause of the deviation. Laser-based particle size measurements and thermophoretic sampling in low strain rate flames show that the particles have diameters between 10 nm and 30 nm. Thermophoresis affects the nanoparticle distribution in the flames, in some cases causing particles to cross the stagnation plane. The scattering magnitude in the counterflow diffusion flames appears to be strongly dependent on the residence time, and relatively independent of the peak flame temperature.

INTRODUCTION

Production of the widely used but ozone-destroying compound CF_3Br has been banned, and there remains a need for alternative fire suppressants in a variety of applications. Because some metal compounds have been shown to be up to two orders of magnitude more effective than CF_3Br at reducing the burning velocity of premixed flames [1, 2], it is of interest to understand their mechanisms of inhibition to determine if there are ways that they might be used as additives to fire suppressant blends, particularly for unoccupied spaces.

In previous research, a gas-phase mechanism for inhibition by $Fe(CO)_5$ [3] and ferrocene [4] was developed, and it predicted the observed strong inhibition at low inhibitor mole fraction reasonably well for many test conditions [5]. For the premixed flames, the dramatic loss of effectiveness of these iron compounds at volume fractions above about 100 ppm[1] was shown to be caused by the condensation of iron-containing intermediates, and the subsequent formation of particles [6] (with particle residence time more important than peak flame temperature). While good progress has been made in understanding the behavior of these compounds in premixed flames [6, 7], fires are diffusion flames, and it is important to extend the tests to more representative conditions.

In recent experimental studies with diffusion flames [2], $Fe(CO)_5$ showed strong inhibition under certain conditions, but almost none under others. Addition of $Fe(CO)_5$ to the oxidizer stream of a methane-air counterflow diffusion flame produces a large change in the extinction strain rate, whereas addition to the fuel stream yields virtually no effect. In diffusion flame experiments with diluted fuel vs. oxygen-enriched air, subsequent numerical modeling using a gas-phase mechanism [3] explained only

*Corresponding author. E-mail: linteris@nist.gov

†Currently at Cleaire Advanced Emission Controls, 14775 Wicks Blvd., San Leandro, CA 94577-6779.

☆Official contribution of the National Institute of Standards and Technology, not subject to copyright in the United States.

[1] All uses of ppm in this paper are on a volume basis and correspond to μL/L.

COMBUSTION AND FLAME 128:145–164 (2002)

Published by Elsevier Science Inc.

0010-2180/02/$–see front matter
PII 0010-2180(01)00341-8

some of the experimental results (e.g., predicting much stronger inhibition for many conditions than was observed in the experiments). Furthermore, addition of $Fe(CO)_5$ to the air stream of either counterflow diffusion or premixed flames illustrates a difference in behavior in the two. In premixed flames, there is a dramatic change in the inhibition behavior of the $Fe(CO)_5$ at about 100 ppm, with the burning velocity vs. $Fe(CO)_5$ mole fraction curve appearing very steep below 100 ppm, but nearly flat above that value (the ratio of slopes above and below 100 ppm is about 100). For counterflow diffusion flames, the extinction strain rate vs. $Fe(CO)_5$ mole fraction curve *also* experiences a large change in slope near 100 ppm, but the reduction in the effectiveness of the $Fe(CO)_5$ (i.e., the change in slope) is much milder, about a factor of seven. The goal of the present work is to understand the role of particles in the loss of effectiveness of $Fe(CO)_5$ in the counterflow diffusion flames and provide insight into the shortcomings in the gas-phase only numerical model.

Counterflow diffusion flames—as compared with premixed flames—provide a flexible environment for inhibitor addition, and consequently have been widely used in studies of fire suppressant effectiveness [8–12]. In premixed flames, all of the inhibitor flows directly into the reaction zone, whereas in counterflow flames, the amount of the inhibitor that reaches the flame is dependent upon the location of inhibitor addition relative to the locations of the flame and stagnation plane (as discussed in more detail below). Building upon the traditional co-flow diffusion flame experiments of Simmons and Wolfhard [13], several recent studies have systematically added chemical inhibitors to either the fuel or oxidizer stream of counterflow flames [10, 14–18]. Additional studies have also been conducted with agent addition to either stream but with variable mixture fraction (i.e., flame location) [2, 19], so that the inhibitor reaches the main reaction zone either by convection or diffusion.

Recently, counterflow diffusion flames have also been used as reactors for particle synthesis. The studies described in the review of Wooldridge [20] are of value to the current study. However, since the strain rates in those particle synthesis flames have typically been between 10 s^{-1} and 20 s^{-1} (i.e., 20–30 times lower than in the current investigation), the resulting shorter residence times must be considered when comparing between experiments.

In this paper we investigate iron-species condensation in non-sooting CH_4-O_2-N_2-$Fe(CO)_5$ counterflow diffusion flames to determine the effect of particle formation on flame inhibition. We use laser-light scattering to determine particle size and location, and thermophoretic sampling for particle morphology. Flame conditions are chosen to clarify the relative effects of residence time and peak flame temperature on particle formation. Calculated flame structures from one-dimensional gas-phase flame models assist in the interpretation of the experimental data and provide insight into the particle formation processes.

EXPERIMENT

The counterflow burner system has been described previously [2, 21]. The fuel and oxidizer tubes (22.2-mm diameter) are separated by 11 mm, and there is a nitrogen shroud flow from a concentric cylinder (51-mm diameter) around the bottom (oxidizer) jet. The burner produces a non-sooting flame with a flat region in the center. The strain rate a (the derivative of the velocity with respect to the axial position) is approximated from the outer flow jet exit velocities as $a = (2|V_o|/L)(1 + |V_F|\sqrt{\rho_F}/|V_o|\sqrt{\rho_o})$, where L is the jet separation distance, V_i is the velocity of gas i (F = fuel, O = oxidizer), and ρ_i is the density of gas i [22]. The jet exit velocities are chosen so that the momentum of the two streams is balanced at all values of the strain rate; that is, $\rho_F V_F^2 = \rho_o V_o^2$. Iron pentacarbonyl is added to the flames by diverting part of the nitrogen (or methane) stream to a two-stage saturator maintained in a bath at 17°C to 21°C, held to within ±0.5°C. The gas flow control system and tests to verify carrier gas saturation by $Fe(CO)_5$ have been described in a previous publication [5], and the optical system has been described in a related paper covering particle measurements in premixed

flames [6]. The laser-based measurements are made along a vertical profile at the centerline of the fuel and oxidizer tubes, and the scattering calibration is performed with blends of CH_4 and N_2 (scattering cross sections of 18.68×10^{-28} cm^2 and 8.69×10^{-28} cm^2 at 488 nm, respectively [23]). The path length for the laser extinction measurements (effectively doubled by a retro-reflection technique [6]) is (4.4 ± 0.4) cm.

Data Reduction

The optical detection system measures the laser light scattered by molecules and particles at the beam waist and the attenuation of the laser beam through the flame. Combined with the calibration data, these measurements provide the scattering cross section for vertically polarized light Q_{vv} and extinction coefficient k_{ext}, and allow calculation of particle diameter, volume fraction, and number density. In terms of the measured quantities, the scattering cross section and extinction coefficient are

$$Q_{vv} = Q_{vv,cal}\frac{S_{vv}}{S_{vv,cal}}\frac{\tau_{cal}}{\tau_\lambda} = C\frac{S_{vv}}{\tau_\lambda} \quad \text{and}$$

$$k_{ext} = \frac{1}{L_o}\ln\frac{1}{\tau_\lambda},$$

where S_{vv} is the signal strength from the optical detector, τ is the transmissivity, and L_o is the pathlength of the laser beam through the flame; the subscripts λ and *cal* refer to the results at hand and with the calibration gases. The data reduction procedure also requires the refractive index (m) of the particles and a particle size distribution function. We do not know the composition of the iron particles (as will be discussed below), but the refractive indices at 488 nm have been reported for several iron-containing particles: Fe (2.40–3.54i) [24], FeO (2.13–0.69i) [25], and Fe_2O_3 (1.64–0.30i) [25]. A log-normal particle size distribution is a reasonable approximation since it has been found to be appropriate for nucleating metal particles in inert gas evaporation systems [26], nucleating oxide particles in flames [27, 28] and composite soot-iron particles in flames [25, 29]. We use a zeroth-order log-normal distribution, which is given by

$$p(r) = \frac{1}{N_t}\frac{dN}{dr} = \frac{1}{\sqrt{2\pi}r\ln\sigma_g} \cdot \exp\left[\frac{-(\ln r - \ln r_g)^2}{2(\ln\sigma_g)^2}\right]$$

where N is the number of particles at a radius r, and N_t is the total number of particles. For a log-normal distribution, the count mean radius is equal to the geometric mean radius r_g, which is defined by $\ln r_g = \int p(r)\ln(r)dr$. The geometric standard deviation σ_g is defined [30] by $\ln\sigma_g = [\int p(r)(\ln(r) - \ln r_g)^2 dr]^{1/2}$.

The mean extinction and differential scattering cross sections are defined as $k_{ext} = N_t \int_0^\infty C_{ext}(r)p(r)dr$ and $Q_{vv} = N_t \int_0^\infty C_{vv}(r)p(r)dr$ where $C_{ext}(r)$ is the extinction cross section for a single particle of radius r, and $C_{vv}(r)$ is the scattering cross section for a single particle of radius r for vertically polarized light. For a log-normal size distribution of particles, it is possible to analytically integrate the k_{ext} and Q_{vv} equations for particles in the Rayleigh scattering regime [25], resulting in

$$k_{ext} = N_t\left(\frac{8\pi^2}{\lambda}\right)E(m)r_g^3\exp\left[\frac{15}{2}(\ln\sigma_g)^2\right]$$

and

$$Q_{vv} = N_t\left(\frac{2\pi}{\lambda}\right)^4 F(m)r_g^6\exp[24(\ln\sigma_g)^2],$$

where $E(m) = -\mathrm{Im}\left\{\frac{m^2-1}{m^2+2}\right\}$, $F(m) = \left|\frac{m^2-1}{m^2+2}\right|^2$.

The particle volume fraction ϕ_v is $\phi_v = \frac{\lambda k_{ext}}{6\pi E(m)}$.

For our system of equations, there are more unknown variables (N_t, r_g, σ_g) than equations (two), so we must specify one of the variables. Specifying the geometric width of the size distribution is a reasonable approach, since previous research has shown it to be nearly constant across a range of conditions. Granqvist and Buhrman [26] found that for 11 different metals (including Fe) the geometric width of the size distribution of homogeneously nucleated particles fell into a band given by $\sigma_g = 1.48 \pm 0.12$. Although the chemical reactions in the flames of the present paper may have an effect on the nucleation rates, it is not expected to change the

physics of the nucleation process, and the use of σ_g is a reasonable approximation. More important, for flames with relatively high agent concentration and long residence times (as described below) there may be significant agglomeration. Under such conditions, it should be noted that the value of σ_g can be two or higher, which would affect considerably the inferred number density [31]. The volume fraction, of course, is unaffected by variations in σ_g.

Experimental Uncertainty

The uncertainty analysis consists of calculation of individual uncertainty components and rms summation of components [32, 33]. All uncertainties are reported as *expanded uncertainties*: $X \pm U$, where U is ku_c, and is determined from a combined standard uncertainty (estimated standard deviation) u_c, and a coverage factor $k = 2$ (level of confidence ~95%). Likewise, when reported, the relative uncertainty is $U/X \cdot 100\%$, or $ku_c/X \cdot 100\%$. The expanded relative uncertainties for the experimentally determined quantities in this study are as follows: 2% for global strain rate in the counterflow diffusion flames; 5% for the extinction strain rate; and 11.5% for $Fe(CO)_5$ mole fraction.

For the scattering measurements, the combination of steep spatial gradients in the flame, small particle scattering cross section, instability in the flame, and system noise causes the scattering signal to vary about a local mean value at any given location. For each Q_{vv} point in the figures, 100 measurements of S_{vv} were made in 1 s; the maximum standard deviation is generally no more than 10% of the mean in the region of high Q_{vv} and in the unburned reactants. In some cases, however, such as the Q_{vv} of room temperature air, the maximum standard deviation can be up to 20%. The resulting uncertainties in the laser-based particle properties are included in the tables below.

FLAME STRUCTURE

To investigate the effects of flame temperature, residence time, and the location of inhibitor addition on particle formation, we employ three counterflow diffusion flames with two inhibitor addition locations, for a total of six flame configurations. The three flame types are shown schematically in Fig. 1. To describe the flame configuration compactly, we use the notation FX_y-IX, in which the flame location is described by the first half, and the inhibitor location by the second half. Here, "F" and "I" refer the flame and inhibitor and "X" refers to the location of each (fuel stream F, or oxidizer stream O). The parameter "y" denotes a diluted fuel stream (blank for undiluted, subscript *d* for fuel *diluted* with nitrogen and air enriched with oxygen). For example, there are three flame configurations, FO, FO_d, and FF_d as shown in Fig. 1: flame on the oxidizer side, flame on the oxidizer side with diluted fuel, and flame on the fuel side with diluted fuel, respectively. The location of the inhibitor addition is shown schematically on the left side of Fig. 1 as IO or IF, inhibitor added to the oxidizer or fuel side or the stagnation plane, respectively. Thus, the notation FO-IO refers to a *F*lame on the *O*xidizer side, *I*nhibitor added to the *O*xidizer stream, with undiluted fuel. This configuration (the most typical) is produced from streams of undiluted methane and unenriched air. Figure 1 also lists some properties of the flames. The stoichiometric mixture fraction Z_{st} quantifies the location of the flame relative to the fuel and air streams. For $Z_{st} = 0.5$, the flame is coincident with the stagnation plane; for $Z_{st} < 0.5$, the flame is on the oxidizer side of the stagnation plane; and for $Z_{st} > 0.5$, the flame is on the fuel side of the stagnation plane. The first flame, FO, is a stream of methane flowing against air, which results in a flame on the air side of the stagnation plane with a calculated distance of about 1 mm between the peak temperature and the stagnation plane. To produce an environment with the *F*lame on the *F*uel side of the stagnation plane, the third flame, FF_d, uses a stream of *d*iluted fuel flowing against oxygen-enriched air. However, some important properties of the FF_d flame (such as the distance to the stagnation plane and the peak temperature) are significantly different from those in the undiluted FO flame. Hence, we created a third flame (FO_d in the middle of Fig. 1) which, while maintaining the flame on the oxidizer side of the stagnation plane (as in the FO flame), has a peak temperature and distance of the peak temperature from the

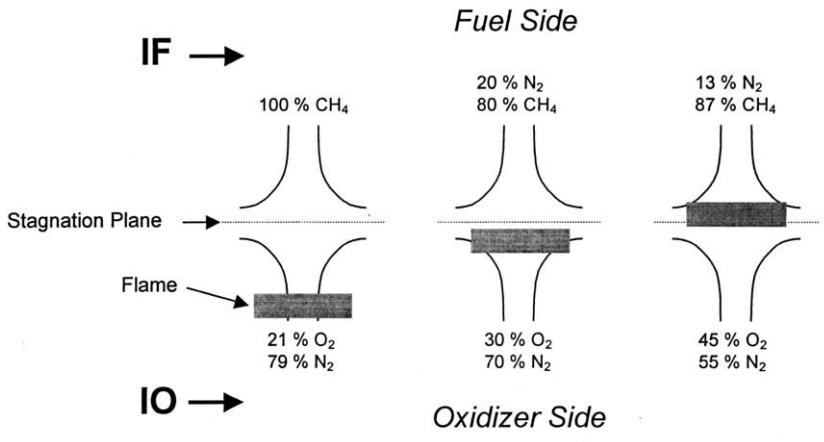

Flame type:	FO	FO_d	FF_d
Z_{st} :	0.055	0.4	0.6
Flame distance below stagnation plane (mm):	0.87	0.20	-0.06
a_{ext} (s^{-1}) :	660	740	766
Total Flow Oxid. (L/min):	22.0	24.6	24.3
" Fuel (L/min):	29.4	26.1	25.9
$T_{max, calc.}$ @ a_{ext} (K):	1786	1630	1590
$T_{max, calc.}$ @ a=200 s^{-1} (K):	2020	1840	1630

Fig. 1. Characteristics of the counterflow flames. Burner jet exit area is 3.87 cm^2, and jet separation is 1.1 cm.

stagnation plane that are more like those of the fuel-side flame FF_d, facilitating comparisons between FO_d and FF_d. (Numerical calculations show that the two diluted-fuel flames described above, FO_d and FF_d, have temperature profiles which are roughly mirror images of one another, symmetrical about the stagnation plane.) Fig. 1 shows clearly the movement of the flame toward and across the stagnation plane with increasing fuel dilution and oxygen enrichment, and the attendant increase in Z_{st}.

To illustrate the differences in the flame structure between the FO, FO_d, and FF_d flames, Fig. 2 shows the calculated temperature and gas velocity profiles for each flame near its extinction strain rate. The diluted-fuel flames have peak temperatures that are roughly 200 K lower than the temperature of a CH_4 versus air flame, which could lead to higher condensation rates since saturation vapor pressure is a strong function of temperature. The diluted-fuel flames are also much closer to the stagnation plane, resulting in lower velocities—and hence higher residence times—in the flame zone. For example, in

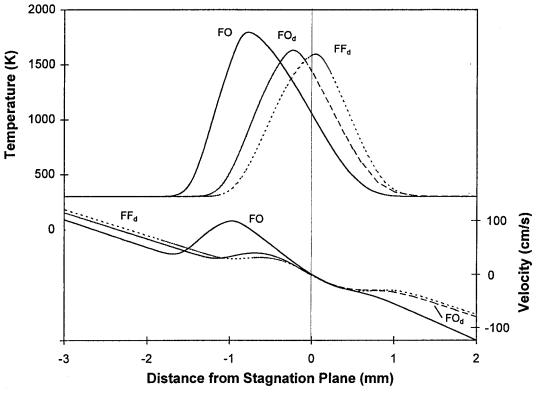

Fig. 2. Calculated temperature and velocity fields for the three flames near their respective extinction points. The strain rates are 532 s^{-1}, 494 s^{-1}, and 488 s^{-1} for the FO, FO_d, and FF_d flame, respectively. The vertical line denotes the stagnation plane.

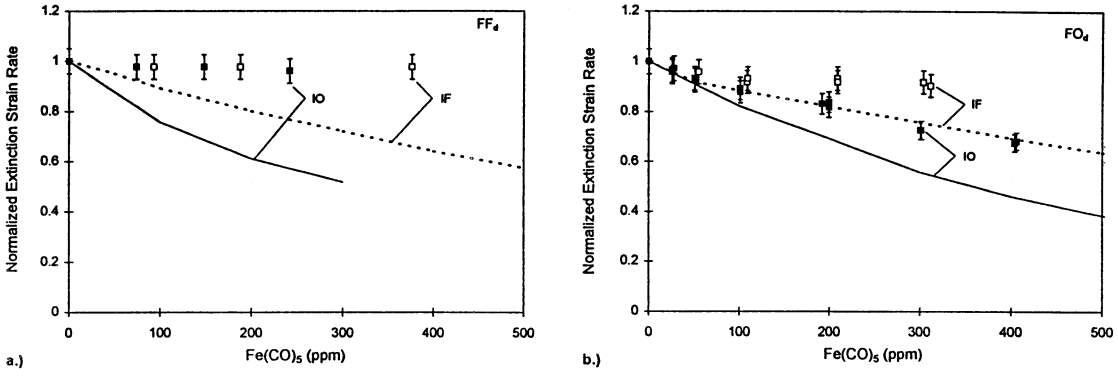

Fig. 3. Measured (points) and calculated (lines) normalized extinction strain rate for diluted fuel versus O_2-enriched-air flames (a) Flame on the fuel side (FF_d), (b) Diluted-fuel flame on the oxidizer side (FO_d). Inhibitor in the fuel: open symbols and dashed lines; inhibitor in the oxidizer: filled symbols and solid lines. Source: ref [34].

the FO flame, the velocity at the point of peak temperature is roughly 100 cm/s, whereas for the diluted-fuel flames it is less than 30 cm/s. The significance of these differences are discussed below.

In the original experiments on $Fe(CO)_5$ in counterflow flames [2], measurements of a_{ext} were made in the FO, FO_d and FF_d flames. In the two diluted-fuel flames, addition of $Fe(CO)_5$ to either the fuel or the oxidizer stream resulted in less reduction (compared to the undiluted FO flames) or no reduction in the measured extinction strain rate. In a subsequent numerical modeling paper [3], it was reported that the gas-phase chemical mechanism strongly overpredicts the inhibition effect in most of the diluted-fuel flames. These experimental and numerical results are illustrated in Fig. 3a (FF_d) and Fig. 3b (FO_d). To determine if the deviation between experiment and model is because of particle formation, light scattering and extinction measurements were made in the flames of Fig. 1 at several conditions. In the next few sections we present the results of the particle measurements, starting with the undiluted flame on the oxidizer side of the stagnation plane (FO), followed by the diluted-fuel flame on the oxidizer side (FO_d)—which has a structure most similar to the FO flame just presented—and concluding with the diluted-fuel flame on the fuel side (FF_d).

RESULTS AND DISCUSSION

Validation of Calculated Temperature Field

In previous work, flame inhibition by $Fe(CO)_5$ in diffusion flames has been studied through measurements of global properties (reactant flows at extinction) [2]. The structures of the flames have been calculated based on a detailed kinetic model, and some validation of the kinetic mechanism has been provided by comparisons between measured and calculated global properties of premixed and diffusion flames [3, 5, 7, 34]. Clearly, detailed measurements of the flame structure can provide the best validation of the mechanism, and while they are desired, they are not yet available for flames inhibited by $Fe(CO)_5$. Nonetheless, we use the calculations to interpret the present particle measurements. In particular, the calculations provide an estimate of the temperature profile, as well as the region of high radical mole fraction and subsequent high activity of the gas-phase iron species catalytic radical recombination cycles.

The temperature profile can be obtained experimentally from the Rayleigh scattering by the cold reactant and hot product gases. Calculating the temperature *from* the Rayleigh scattering signal, however, requires knowledge of the exact species mole fractions at each position in the flame (since it is not possible to separate changes in scattering cross section caused by temperature variation from those caused by

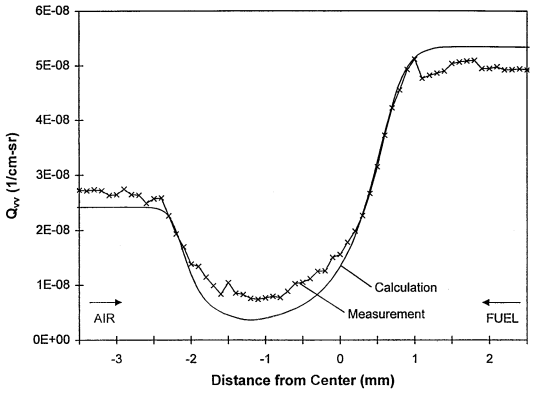

Fig. 4. Comparison of calculated and measured Q_{vv} for uninhibited flame (case FO) at $a = 330\ s^{-1}$.

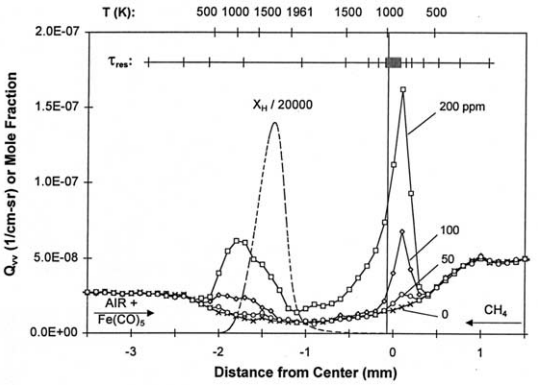

Fig. 5. Methane-air counterflow diffusion flame with inhibitor in the oxidizer (FO-IO). Shown are the calculated temperature (upper scale), stagnation plane location (vertical line), and H-atom mole fraction (dashed line) for the uninhibited flame, and the measured scattering profiles (connected points) for $Fe(CO)_5$ mole fractions of (0, 50, 100, and 200) ppm in the air stream ($a = 330\ s^{-1}$, which is 50% of a_{ext} for the uninhibited flame and 77% of a_{ext} for X_{in} = 200 ppm). The estimated residence time for 5 nm particles is shown as 10 ms intervals in the hatched line near the top.

changes in chemical composition). Alternatively, we can compare the experimental and calculated temperature profiles indirectly, by using the calculated species mole fractions and temperature to evaluate the scattering cross section. The calculations for flame structure are performed using a flame code from Smooke [35], which uses the *Chemkin* [36] and the transport property subroutines [37], and a one-carbon chemical mechanism [38]. At each grid point in the flame, we calculate the density-weighted scattering cross section $Q_{vv,j} = e_o \sum_{i=1}^{ii} \sigma_i X_{i,j}(1/T_j)$, where e_o is the empirically determined optical efficiency coefficient (K/cm^3-sr), σ_i is the Rayleigh cross section of the i-th species (cm^2), $X_{i,j}$ is the mole fraction of the i-th species at the j-th grid point, and T_j is the temperature at the j-th grid point (K). We consider only the major species CH_4, N_2, O_2, CO_2 and H_2O in the summation, and use cross section data from Ref. [23] (CH_4, N_2) and Ref. [39] (O_2, CO_2, and H_2O). We obtain the optical efficiency coefficient of the experimental set-up by a best-fit to the signals from the inlet reactants at the air and fuel jet exits. A comparison of the calculated and measured cross section for an uninhibited flame at a = 330 s^{-1} is shown in Fig. 4. Qualitative agreement is good, notably in terms of the location of initial decrease in Rayleigh cross section, and the location of minimum cross section (i.e., maximum temperature). Despite the discrepancy in the absolute Q_{vv} (believed to be caused mainly by stray scattered light), we can use the numerical calculations to assist in interpretation of the experimental data. For example, the calculations can be used to identify the *spatial* locations of various features on the scattering data, such as the stagnation plane and the region of high temperature.

Laser Scattering Measurements of Particles

In this section we discuss the formation of particles in the three types of counterflow flames, beginning with the undiluted CH_4 versus air (FO), and following with the flames of diluted fuel and O_2-enriched air that are stabilized on the oxidizer side (FO_d) and the fuel side (FF_d) of the stagnation plane. For each flame we present results of the scattering cross section measurements and assess the effect of the particles on flame inhibition.

Flame on Oxidizer Side

Inhibitor in the Oxidizer (FO-IO)

Figure 5 shows the measured scattering cross section (Q_{vv}) together with the calculated temperature (upper x-axis), H-atom mole fraction, and stagnation plane location for CH_4-air flame

with inhibitor in the oxidizer (FO-IO). The strain rate is 330 s^{-1}, which is (50 ± 2.5) % of the extinction strain rate. Unlike in premixed flames, the "thickness" (indicated by the region of increased temperature) of a counterflow flame (when far from the extinction condition) is unaffected by addition of the inhibitor [34]; hence, the Q_{vv} profile of the uninhibited flame (from Rayleigh scattering by the hot products and cold reactants) is a good marker for the flame location, even for inhibited flames. Note that the temperature profile inferred from the Rayleigh scattering result is nearly identical for all amounts of added inhibitor in Fig. 5. Further, although the OH laser induced fluorescence measurements of Skaggs et al. [40] (propane-air counterflow flames, a = 76 s^{-1}) show [OH] profiles to have a narrower full width at half maximum with addition of 1000 ppm of $Fe(CO)_5$, our calculations (methane-air flames, a = 100 s^{-1}, 200 ppm $Fe(CO)_{5)}$ show that narrower OH profiles occur in our flames too—even while the temperature profile and location of the [OH] peak are unchanged.

The hatched horizontal line near the top of Fig. 5 shows the estimated residence time τ_{res} (via 10 ms intervals between hatch marks). The estimation encompasses the gas and thermophoretic velocities (assuming 5 nm particles) as discussed below. Note that near the particle stagnation region, the near-zero particle velocities create large uncertainties in the estimated residence time. This region (caused in part by the limited spatial resolution of the numerical flame structure calculation) is indicated by a shaded bar.

As shown in Fig. 5, at each inhibitor concentration, there are three distinct regions in the flame: (1) a region of particles on the oxidizer side of the flame, (2) a nearly particle-free region near the point of peak temperature, and (3) a region of particles on the fuel side of the flame. As the inhibitor mole fraction increases from 50 ppm to 200 ppm, the scattering increases strongly on both sides of the flame, with a faster increase on the fuel side. This strong dependence of scattering on additive concentration has been observed previously [41, 42]. Also, a double-peaked scattering profile like that in Fig. 5 has been observed in H_2-O_2 counterflow diffusion flames with added $Al(CH_3)_3$ and $TiCl_4$ [43], and $VOCl_3$ and PCl_3 [44]. In those studies, both peaks occur in a region of monotonically rising temperature, and are thought to be a result of changes in particle structure from chains of small particles to relatively large spheres.

The two-peaked structure in the Q_{vv} data of Fig. 5 can be explained through consideration of the calculated temperature (upper x-axis) and flame structure. Inhibitor, entering with the air, decomposes into Fe and CO upon heating. In this relatively low-temperature region, Fe can condense (or oxidize and then condense) resulting in formation of the first peak ($-2.1 < z < -1.8$, where z is the distance from the center of the nozzles). The temperature continues to increase ($-1.8 < z < -1.2$), which may cause a reduction of particle size or number density through evaporation, reducing the scattering cross section. As the gas cools on the fuel side of the peak temperature ($-1.2 < z < 0.4$), the particles reappear and the scattering cross section increases. Because the gas velocity drops as the stagnation plane is approached, the residence time increases and particles grow larger or agglomerate. It is also possible that the different peak heights on the fuel side and air side are caused by thermophoretic redistribution of particles or changing gas composition and the resulting difference in nucleation behavior [41].

We can use the results shown in Fig. 5 to infer the effect of the particles on flame inhibition. The appearance of particles on the oxidizer side is most significant, since that is where the inhibition reactions are believed to be occurring [34]. Hydrogen atom is the radical most scavenged by the iron compounds, so its profile serves as a marker of the region of important inhibition chemistry (note that the *location* of the peak H-atom profile is the same for inhibited and uninhibited flames [34]). The overlap between the H-atom profile and the regions of increased scattering is significant (especially at 200 ppm), and suggests that particle formation influences the inhibition chemistry since the particles are likely composed of inhibiting species from the gas-phase. The fuel-side peak probably has little effect on the inhibition chemistry since the loss of active species to particles

on the fuel side is beyond the region of chemical influence.

At first glance, it is surprising in Fig. 5 that fuel-side peaks occur, since these require particles (or their precursors) to cross the stagnation plane. Larger particles have been measured and predicted to cross the stagnation plane [45, 46]; however, for smaller particles, as in the current study, their location may be a result of thermophoretic movement to the region of lower temperature. We can evaluate this possibility by employing the counterflow flame model. The thermophoretic velocity of a particle can be estimated at each location in the flame via $V_T = (\alpha_T D)_p \cdot (-\nabla T/T)$, where α_T is the (dimensionless) thermophoretic diffusion factor, D is the particle Brownian diffusivity, T is the local temperature, P is the pressure, and ∇T is the local temperature gradient [47]. Waldmann and Schmidt [48] used kinetic theory to develop an approximation for $(\alpha_T D)_p$ which applies to the free molecular regime (Kn $\gg$ 1, where Kn is the ratio of the mean free path to the particle radius): $(\alpha_T D)_p = (3/4) \cdot [1 + (\pi/8 \cdot \alpha)]^{-1} \cdot \nu$, where α is the tangential momentum accommodation coefficient (which we set equal to unity, as justified by Talbot et al. [49]), and ν is the kinematic viscosity (momentum diffusivity) of the local gas mixture (calculated using the *Chemkin* transport libraries [37]). Our measurements suggest that the particles are in the free molecular regime (see the Particle Concentration and Morphology section below). Figure 6 shows calculated gas velocity (V_{gas}) along with the negative of the thermophoretic velocity, and the measured Q_{vv} for $X_{in} = 200$ ppm. Near the air-side scattering peak, V_T is four times smaller than V_{gas}, implying that thermophoresis has a minor effect on the shape of the particle field. Near the fuel-side scattering peak, however, $V_T > V_{gas}$, so that thermophoresis has likely caused the particles on the fuel side of the flame to cross the stagnation plane and move upstream. These results have relevance for material synthesis in counterflow flames. Thermophoretic effects could potentially be used to isolate nascent particles in oxidizing or reducing sections of the counterflow reactor, or could be used as an additional control of the residence time for particle growth. Alternatively, thermophoresis could lead to particle contamination as particles remain in the wrong part of the flame for too long.

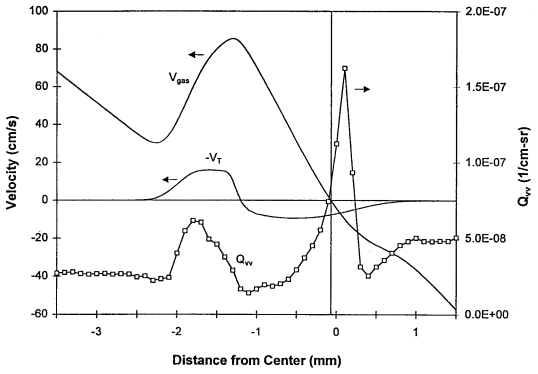

Fig. 6. Measured Q_{vv}, calculated gas velocity V_{gas}, and negative of the thermophoretic velocity ($-V_T$) for case FO-IO. Values of $-V_T > 0$ correspond to particles moving to the left. The vertical line marks the stagnation plane. The location of $V_T = 0$ at $z = -1.2$ mm corresponds to the point of peak temperature. $a = 330\ s^{-1}$, $X_{in} = 200$ ppm.

One of the primary motivations for the present particle measurements is to understand why the numerical calculations using the gas-phase mechanism significantly overpredict the inhibition by $Fe(CO)_5$ in FO-IO flames. As described in Ref. [3], the inhibition calculated using a gas-phase mechanism is within experimental uncertainty for X_{in} below about 50 ppm, but above that value the model predicts too much inhibition. It has been proposed that particle formation is a reason for the discrepancy, so it is of interest to see how particle formation and the deviation between model and experiment correlate.

To compare the presence of particles and the strength of the flame inhibition, we must define suitable parameters describing each variable. The extinction strain rate (a_{ext}) is defined by the global relationship above using the jet exit velocities at which the flame extinguishes, and a_{ext} can be used as a measure of the effect of the inhibitor on the overall reaction rate, since with added $Fe(CO)_5$, the flame location does not change significantly. (As described previously [10], changes in the flame location with inhibitor addition can change the scalar dissipation rate—which is a truer measure of the characteristic chemical time than the extinction strain rate). For the 'particle parameter,' we desire a measure of the presence of particles at (or very

close to) the extinction condition. In the present work, we use the peak scattering cross section Q_{vv} as an estimate of the particle quantity (since other measurements of particle loading are difficult in the present flames, as described below). Also, for the FO-IO flames, we only examine the oxidizer-side peak since formation of particles on the fuel side of the flame is downstream of the location where the important inhibition chemistry is believed to be occurring.

In principle, we could determine the scattering cross section very close to extinction. Such measurements are difficult, however, since the flame is unstable there. It is possible to gain some understanding of behavior near extinction by examining the behavior at stable strain rates that are below extinction, and then extrapolating to the strain rate at extinction. The extrapolated peak Q_{vv} at the extinction strain rate of 660 s^{-1} is $6 \cdot 10^{-8}$ cm^{-1} sr^{-1} and $9 \cdot 10^{-8}$ cm^{-1} sr^{-1} on the air and fuel side, respectively. These values are still significantly above the Q_{vv} from the reactant gases in the uninhibited flame at the same spatial location ($\approx 2 \cdot 10^{-8}$ cm^{-1} sr^{-1}), implying that the particles do not completely disappear at the extinction point. Alternatively, measurements at a fixed strain rate (Fig. 5) are possible, but would be inappropriate because at a = 330 s^{-1} the 0 ppm flame is far from extinction while the 200 ppm flame is close to extinction, and the scattering signal decreases as one gets close to extinction. As an illustration, for a flame with 200 ppm of $Fe(CO)_5$, increasing the strain rate from 150 s^{-1} to 350 s^{-1} decreases the air-side peak Q_{vv} by a factor of 2.9 (This occurs despite the decrease in peak temperature which accompanies the increase in strain rate, suggesting that for these conditions, particle formation depends more upon changes in the residence time than the peak temperature.) It is most appropriate to choose flames that are at the same *relative strain rate* with respect to extinction (a/a_{ext}), as close as possible to extinction. As a compromise, for our correlation of the particle scattering with the degree of chemical inhibition, we make our scattering measurements at 75% of the extinction strain rate, as listed in Table 1.

Figure 7 shows the correlation between inhibition (measured and predicted normalized extinction strain rate) and particle formation (peak Q_{vv}) for the FO-IO flame (the calculated and experimental extinction strain rates are each normalized by their uninhibited value). At X_{in} = 100 ppm, where the model predictions are close to the experimental results, there is little more scattering in the inhibited flames than in the uninhibited flame. (The Q_{vv} of the uninhibited flame, from Rayleigh scattering from the gas molecules is roughly 10^{-8} cm^{-1} sr^{-1} at the location of the Q_{vv} peaks in the inhibited flames.) As X_{in} increases and the difference between the measured and predicted extinction strain rate widens, the maximum Q_{vv} increases sharply, thus suggesting that particle formation is the cause of the deviation. As in the premixed flames [6], the active inhibiting species are being lost to the condensed phase particles (which remove radicals at a much slower rate, if at all).

TABLE 1

Measured Values of $0.75 \cdot a_{ext}$ for Various Inhibitor Loadings

$Fe(CO)_5$ (ppm)	a (s^{-1})		
	FO-IO	FO_d-IO	FO_d-IF
0	495	555	555
25	478	534	532
50	431	516	525
100	386	491	506
200	323	460	506
300	298	398	499
400	282	373	—
500	255	351	—

Relative uncertainty of $0.75 \cdot a_{ext}$ is ±5%.

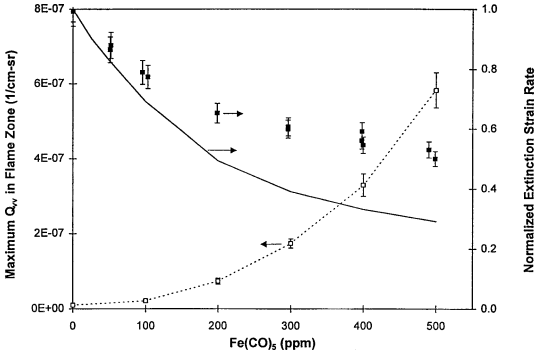

Fig. 7. Correlation between inhibition effect and maximum Q_{vv} (case FO-IO). Filled points are experimental normalized a_{ext}, solid line is calculated a_{ext} ([3]). Open symbols connected by dotted lines are maximum measured Q_{vv}. Particle data collected at 75% of a_{ext} (see Table 1).

While it has been proposed [34] that the reduced effectiveness at high X_{in} could be a result of saturation of the catalytic cycles (because of radical mole fractions approaching equilibrium values and a smaller radical pool), the inhibitor loses its effectiveness more drastically in the experiments than in the calculations (which include the effects of catalytic cycle saturation).

One unexplained difference between the premixed and counterflow results is that the premixed flames have a nearly flat leveling-off behavior at high X_{in}, while in the counterflow flames (filled squares in Fig. 7) the slope is only reduced. While it is difficult to fully identify the reasons without detailed modeling of the condensation process, differences in the time-temperature history of the particles may be significant. For example, in counterflow flames near extinction, higher X_{in} corresponds to higher peak temperature and lower residence time, both of which reduce particle formation rates. Thus, in these counterflow diffusion flames, as inhibitor is added, properties of the flame are modified so as to retard particle formation. Conversely, in premixed flames, as X_{in} increases, the peak temperature is relatively unchanged, but the residence time increases (because of the lower burning velocity), so that flame characteristics for particle formation are enhanced. It is noteworthy that for a CH_4–air flame with 300 ppm of $Fe(CO)_5$, *premixed flames*—which lose their effectiveness more dramatically than do counterflow flames—have a peak scattering signal about twice that of the counterflow flames.

Inhibitor in the Fuel Stream (FO-IF)

With the flame on the oxidizer side of the stagnation plane, addition of $Fe(CO)_5$ to the fuel stream results in no appreciable inhibition [2]. Although a case has been made (using a numerical model with a gas-phase chemical mechanism) that poor transport of the inhibiting molecules to the region of high radical concentration is the most important factor [34], particle formation may have an additional effect. Consequently, scattering cross section measurements were made in flames with inhibitor added to the fuel stream.

Figure 8 shows the scattering cross section resulting from addition of $Fe(CO)_5$ (0 ppm to 300 ppm) to the fuel stream. Most of the scattering occurs on the fuel side of the stagnation plane ($z \approx 0.25$ mm), far away from the point of peak H atom ($z \approx -1.4$ mm). Although this implies that there is no direct overlap between the particle and high radical mole fraction regions, the particles still act as a sink for the inhibiting species, and reduce the number of iron-containing molecules that are available to diffuse through the flame to the region of high radical concentration.

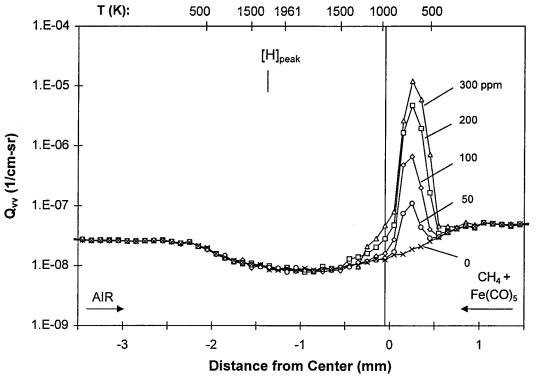

Fig. 8. Measured scattering profiles in CH_4-air counterflow diffusion flame with inhibitor in the fuel (case FO-IF). The calculated temperature and point of peak H-atom mole fraction are marked on the upper x-axis, and the vertical line denotes the calculated location of the stagnation plane. Strain rate = 330 s^{-1}.

The peak Q_{vv} is strongly dependent on X_{in}, but the spatial location of the peak value is independent of X_{in}, a behavior that was previously seen for silica particle synthesis in H_2-O_2 counterflow diffusion flames [41]. Compared to scattering cross section profiles for the FO-IO flame in the previous section, only one peak appears and the maximum Q_{vv} is about 30 times larger. The value of the peak Q_{vv} may be higher because the fuel-side particles have a relatively long residence time, which is because of a combination of low gas velocity near the stagnation plane and a thermophoretic force that opposes the convective flow.

Flame on the Oxidizer Side (diluted)

Inhibitor in Oxidizer Stream (FO_d-IO)

Fig. 9 shows measured Q_{vv} for this flame (FO_d) with inhibitor added to the oxidizer (IO, filled symbols) or the fuel (IF, open symbols) at a =

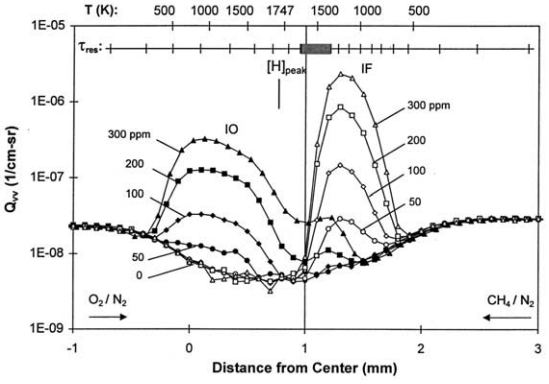

Fig. 9. Measured scattering cross section (log scale) for diluted-fuel flame on the oxidizer side (FO_d) of the stagnation plane at strain of 370 s^{-1} (which is 50% of the a_{ext} for the uninhibited flame). Data are for inhibitor addition to the oxidizer (IO, filled symbols) or to fuel (IF, open symbols). The calculated temperature and point of peak H-atom mole fraction are marked on the upper x-axis, and the vertical line denotes the calculated location of the stagnation plane. The estimated residence time for 5 nm particles is shown as 10 ms intervals in the hatched line near the top.

370 s^{-1} (50% of a_{ext} for the uninhibited flame). With inhibitor in the oxidizer stream, significant scattering appears at X_{in} as low as 50 ppm, indicating rapid particle formation. Compared with the FO-IO flame (linear Q_{vv} scale, Fig. 5), the particle region in the FO_d-IO flame (log Q_{vv} scale) is slightly wider (about 1 mm vs. 0.7 mm), and the peak Q_{vv} is about twice as high as the air-side peak in the FO (Table 2). Inspection of the calculated temperature (upper x-axis of Fig. 5 and Fig. 9) reveals that in both cases most of the particles form at temperatures far below the maximum temperature (between 500–1300 K), implying that the lower peak temperature of the FO_d flame (as compared with FO-IO) is not an important factor for particle formation. Instead, a difference appears to be in the residence time (see Fig. 2); the gas velocity in the region of particle scattering is between 40 cm/s and 100 cm/s in the FO flame, but only 30 cm/s in the FO_d flame. In Fig. 9, the local minimum in Q_{vv} occurs near the point of peak temperature. The calculated peak H-atom location is near the local Q_{vv} minimum, just on the oxidizer side of the stagnation plane. Some overlap between the particles and H-atom profile is apparent, but just as important, the formation of particles upstream of the H-atom region could also reduce the inhibition by sequestering the inhibiting molecules into particles, where they remain until being swept out of the flame zone at the stagnation plane as explained below.

TABLE 2

Peak Q_{vv} in Each Flame Configuration with 200 ppm of $Fe(CO)_5$ Added to One Stream

Flame configuration	Peak Q_{vv} (10^7 cm^{-1} sr^{-1})	Strain Rate (s^{-1})
FO-IO (air side peak)	0.6	330
FO-IO (fuel side peak)	1.6	330
FO_d-IO	1.2	370
FF_d-IO	3	383
FO-IF	47	330
FO_d-IF	8.6	370
FF_d-IF	4	383

As in the FO-IO flame, thermophoresis has an effect on the Q_{vv} profile, especially near the stagnation plane ($z \approx 1.0$). Figure 9 shows that some scattering occurs on the fuel side of the stagnation plane for X_{in} = 200 ppm and 300 ppm for addition of inhibitor to the oxidizer. As with the FO-IO flames, we turn to numerical modeling to assist in explaining this result. For uninhibited FO_d flames, comparison of the calculated and measured scattering cross section again implies that the temperature field is well predicted by the calculations. The calculated thermophoretic and gas velocity (Fig. 2) for the FO_d flames shows that V_T is significantly higher than V_{gas} near the stagnation plane, resulting in a thermophoretic transport of particles toward the fuel jet, and the appearance of particles on the fuel side of the stagnation plane.

Inhibitor in Fuel Stream (FO_d-IF)

When the inhibitor is added to the fuel (IF, Fig. 9), Q_{vv} is significantly higher; e.g., addition of 300 ppm of $Fe(CO)_5$ to the fuel yields a peak scattering signal nearly seven times higher than for addition to the oxidizer. Also, the Q_{vv} profile is spatially narrower for the inhibitor added to the fuel rather than the oxidizer stream, as in the FO-IO vs. the FO-IF flames. Thermophoresis near the stagnation plane drives particles upstream toward the fuel side, leading to a somewhat steeper decrease in Q_{vv} than would occur otherwise. The longer particle residence times for agent added to the fuel side are

indicated by the hatched bar at the top of Fig. 9, which shows about a factor of two increase in τ_{res} as compared to air-side agent addition.

Comparing the oxidizer-side peak Q_{vv} in the FO_d-IF condition with that for the FO-IF condition, we see that the peak Q_{vv} is about 5 times lower for FO_d-IF (Table 2). The reason for this may be related to the time-temperature history of the nascent particles in each flame. The particles in the FO_d-IF start to form about 0.75 mm from the stagnation plane, where the calculated velocity is roughly 30 cm/s. While the gas decelerates, the temperature is increasing, and reaches about 1,600 K at the stagnation point. That is, the region of low velocity corresponds to a high gas temperature, and is thus unfavorable for rapid condensation. In the FO-IF, the gas velocity is also about 30 cm/s at the point of first particle formation, but the temperature is lower, only 1,000 K near the stagnation plane (i.e., the FO flame is further upstream on the oxidizer side than is the FO_d flame). This coincidence of the stagnation plane with a region of favorable temperature for condensation leads to enhanced particle formation in the FO-IF, despite a higher peak flame temperature. Indeed, the FO_d-IF flames (open symbols in Fig. 3b), with less particulate scattering, also show more inhibition in the experiments than do the FO-IF flames [2].

As with the previous flames, it is of interest to see how particle formation and the inhibition measurements correlate for these diluted-fuel flames. For strain rates that are 75% of the extinction strain rate (Table 1), the Q_{vv} was measured in flames with inhibitor loadings up to 500 ppm, and the maximum Q_{vv} in the flame zone is again used as the measure of the presence of particles. In Fig. 10, these maximum Q_{vv} are plotted together with the measured and predicted normalized extinction strain rate. The behavior for both IO and IF are similar in that the calculated and measured normalized extinction strain rates are reasonably close for low $Fe(CO)_5$ mole fraction, but as X_{in} increases, the model overpredicts the inhibition effect. The Q_{vv} is small where the model and experiment agree, but is much larger where there is stronger disagreement between the model and experiment, providing evidence that particle formation causes lower than expected inhibition.

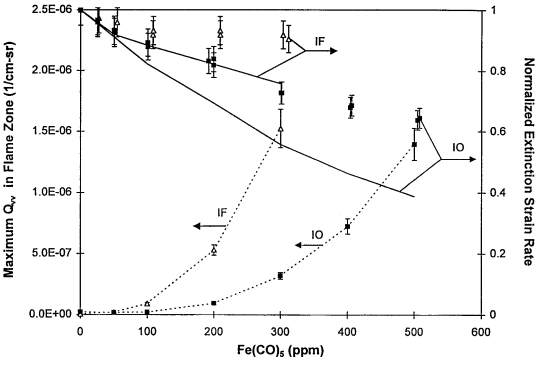

Fig. 10. Normalized experimental extinction strain rate (no lines) and scattering results (dotted lines connecting the points) versus $Fe(CO)_5$ input for diluted flames on the oxidizer side (FO_d) of the stagnation plane. Inhibitor in the fuel: open triangles; inhibitor in the oxidizer: filled squares; upper two solid lines, calculated normalized a_{ext}.

Flame on the Fuel Side (diluted)

Of the three flames examined in this paper, the calculated temperature profile of the fuel-side flame (FF_d) is the most symmetric around the stagnation plane, with the calculated peak temperature just 0.1 mm on the fuel side of the stagnation plane (Fig. 2). Consequently, the measurements of Q_{vv} are also quite symmetric with respect to inhibitor addition location. Figure 11 shows that throughout most of the relevant high temperature region before the stag-

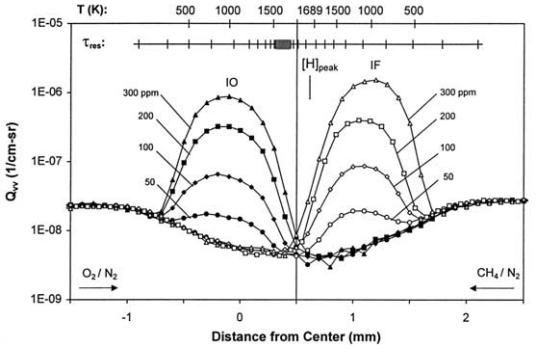

Fig. 11. Scattering profiles through flame on the fuel side (case FF_d) of the stagnation plane. The calculated temperature and point of peak H-atom mole fraction are marked on the upper x-axis, and the vertical line denotes the calculated location of the stagnation plane. Data are for addition of inhibitor to the oxidizer (IO, filled symbols) or to the fuel (IF, open symbols). Strain rate = 383 s^{-1}. The estimated residence time for 5 nm particles is shown as 10 ms intervals in the hatched line near the top.

nation plane, there is a significant scattering signal, which increases as X_{in} increases. A nearly particle-free region, such as that seen by Gomez and Rosner [47], appears around the stagnation plane, but the high strain rate (20 times higher than Gomez and Rosner's) causes the region to be very narrow. Referring to Table 2, for inhibitor addition to the oxidizer (IO), the fuel-side flames (FF_d) produce particles with Q_{vv} about twice as high as the oxidizer-side flames (FO_d). For inhibitor addition to the fuel (IF), the peak Q_{vv} in the fuel-side flames (FF_d) is much smaller than in the oxidizer-side flames (FO_d). These differences are probably a result of the relative positions of the flame and the stagnation plane. For example, in the FF_d-IF flame, the peak Q_{vv} occurs in a region with gas velocity about 30% larger than the velocities in the FO-IF and FO_d-IF flames, resulting in a shorter residence time. Near the stagnation plane, where V_T is comparable to V_{gas}, thermophoresis removes particles from the stagnation region. Additionally, thermophoresis may be the cause of the slight shift of the point of peak Q_{vv} in the IF curves toward the unburned fuel/N_2 mixture jet as X_{in} increases. The steeper temperature gradient on the fuel side of the flame than on the oxidizer side may result in a higher thermophoretic velocity.

The calculated location of the peak H-atom mole fraction occurs between the scattering peaks, as shown in Fig. 11. For inhibitor added to the oxidizer side (IO), formation of the particles upstream of both the flow and particle stagnation planes reduces transport of the particles (and hence the inhibiting species) to the region of high H-atom mole fraction across the stagnation planes. For inhibitor added to the fuel side (IF) there is still significant overlap of the particle region with the H-atom profile (note the scale change between Fig. 5 and Fig. 11). In both the IO and IF cases of Fig. 11, thermophoresis pushes the particles away from the particle stagnation plane. Because the actual temperature field is 2-D, it is possible that the particles also get pushed away from the centerline of the burner. Hence, the mole fraction of iron-containing species on the centerline at the stagnation plane may be low because of particles being swept away by a combination of convection and thermophoresis in the 2-D flow field.

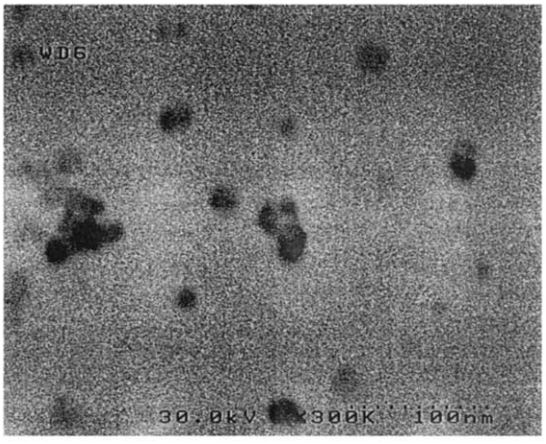

Fig. 12. Electron micrograph of iron-containing particles extracted from counterflow diffusion flame at a = 150 s^{-1} and X_{in} = 300 ppm.

Particle Concentration and Morphology

Thermophoretic Sampling and Microscopy

Thermophoretic sampling of the FO-IO flame seeded with 300 ppm of $Fe(CO)_5$ in the air stream was performed using the apparatus described in ref [6]. The thermophoretic grid (3 mm diameter, which is wider than the flame), was inserted into the center of the region of maximum visible emission of the flame, at the centerline of the burner, and perpendicular to the plane of the flame. Figure 12 shows a transmission electron microscopy (TEM) image of particles sampled from the low strain (a = 150 s^{-1}) counterflow diffusion flame. In general, the degree of agglomeration is much smaller than that of the premixed flame. Primary particle sizes range from 5 nm to 25 nm in diameter, which agrees reasonably well with the laser based measurements described below (given the uncertainty in particle refractive index).

Laser-Light Scattering and Extinction

Laser scattering and extinction measurements together can provide detailed information about the particles. Measurements near flame extinction, however, are challenging in the present flames because of the small particle loading and

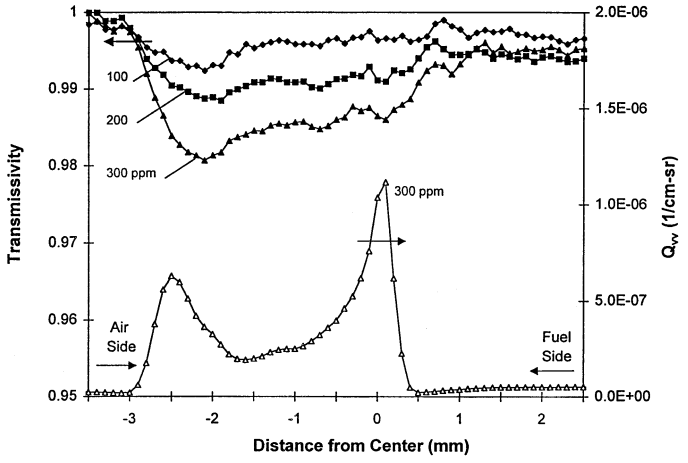

Fig. 13. Transmissivity in low strain rate (a = 150 s^{-1}) flames (case FO-IO) with 100 ppm to 300 ppm. Also shown is a scattering cross section profile for 300 ppm.

subsequent high transmissivity (>99.8%). Nonetheless, it is possible to obtain the size, number density, and volume fraction of the particles slightly away from extinction, and these are described below.

Part of the difficulty in the light extinction measurement arises from the steep temperature gradients in the counterflow flames, which cause significant beam steering and distortion. These deleterious effects are minimized through the use of an integrating sphere and a retro-reflection technique. Fortunately, the beam steering that remains occurs at the outer edges of the high-temperature reaction zone (the maximum is probably between 400 K and 500 K [50]), whereas the lowest transmissivity (highest particle volume fraction) occurs when the temperature is above about 800 K, where beam steering is minimal. Unfortunately, extinction measurements were still not feasible in the counterflow flames presented thus far (a $\approx$ 330 s^{-1}) because of the low absorptivity of the particle field (<0.2%). At low strain rate (<250 s^{-1}) and $Fe(CO)_5$ volume fraction above 100 ppm, however, enough laser extinction occurs so that measurements are possible, and we use measurements made under these conditions to obtain insight into particle formation.

FO–IO Flames

Figure 13 shows the measured transmissivity through FO-IO counterflow flames at a = 150 s^{-1} and various $Fe(CO)_5$ loadings. For reference, the scattering profile for X_{in} = 300 ppm is also shown. The transmissivity drops sharply near the onset of the air-side scattering region, increases between the scattering peaks, and decreases slightly at the fuel side scattering peak. Note that the minimum transmissivity is only 0.98 at 300 ppm, and over 0.99 at 100 ppm. After the fuel-side scattering peak, the transmissivity should approach unity, but edge effects in the bowl-shaped flame cause a small amount of laser extinction (suction from the heat exchanger above the flame curves the edges, but the flame remains flat in the center). As the iron-laden gases contact the cold shroud flow it is possible that increased particle formation and growth occurs at these edges, and causes the beam extinction. Based on visual observations of the flame shape, we estimate that the extinction caused by post-flame gases occurs well beyond the air-side scattering region (z > −0.5), so that the transmissivity data related to the air-side particles are not tainted by the edge effects. For the fuel-side, however, the transmissivity would probably have been higher if the flame were not curved at the periphery.

The edge effects and the near-unity transmissivity described above make extensive plots of particle size and number density as a function of position inappropriate; instead we present limited results in tabular form as discussed in Table 3 below. For five of the six flame configurations,

TABLE 3

Measured Particle Properties for the Six Inhibited Counterflow Flames. The Data Reduction is Performed Assuming FeO Particles with $\sigma_o = 0.39$

Flame	Strain rate (s^{-1})	$Fe(CO)_5$ (ppm)	Mean diameter (nm)	Q_{vv} ($*10^7$/cm-sr)	Number density ($*10^{-10}$ cm^{-3})	Extinction co-efficient ($*10^3$ cm^{-1})	Volume fraction ($*10^8$)
FO-IO (Air pk)	150	100	5.9 ± 0.7	0.65 ± 0.1	9.0 ± 6.9	1.2 ± 0.44	1.6 ± 0.59
	150	200	7.8 ± 0.6	2.4 ± 0.13	6.2 ± 3.4	1.9 ± 0.51	2.5 ± 0.68
	150	300	8.7 ± 0.5	5.4 ± 0.63	7.5 ± 3.0	3.1 ± 0.59	4.1 ± 0.79
	250	300	7.8 ± 0.8	1.6 ± 0.12	4.5 ± 3.1	1.3 ± 0.46	1.7 ± 0.61
FO-IO (Fuel pk)	150	100	8.2 ± 0.8	1.6 ± 0.12	3.3 ± 2.3	1.1 ± 0.4	1.5 ± 0.53
	150	200	9.8 ± 0.6	5.2 ± 0.34	3.5 ± 1.7	2.1 ± 0.49	2.7 ± 0.65
	150	300	11.0 ± 0.5	11 ± 0.63	3.9 ± 1.3	3.2 ± 0.54	4.3 ± 0.72
	250	300	8.8 ± 0.4	4.8 ± 0.33	6.1 ± 2.2	2.6 ± 0.46	3.5 ± 0.62
FO-IF	150	100	17.7 ± 2.2	16 ± 1.8	0.31 ± 0.27	1.1 ± 0.46	1.4 ± 0.61
	150	200	31.5 ± 2.9	110 ± 15	0.070 ± 0.045	1.4 ± 0.43	1.8 ± 0.57
	150	300	33.9 ± 4.4	140 ± 38	0.055 ± 0.046	1.3 ± 0.52	1.8 ± 0.7
	250	300	30.8 ± 3.1	120 ± 9.8	0.087 ± 0.064	1.6 ± 0.58	2.1 ± 0.77
FO_d-IO (Air pk)	150	100	7.3 ± 0.8	1.3 ± 0.13	5.2 ± 3.9	1.3 ± 0.47	1.7 ± 0.62
	150	200	9.5 ± 0.5	8.2 ± 0.91	6.6 ± 2.5	3.6 ± 0.65	4.7 ± 0.86
	150	300	11.6 ± 0.5	20 ± 1.6	5.1 ± 1.6	4.9 ± 0.72	6.6 ± 0.96
	250	300	9.4 ± 0.4	12 ± 0.93	11 ± 3	5.4 ± 0.73	7.2 ± 0.97
FO_d-IF	150	100	9.6 ± 2.3	4.3 ± 0.64	1.2 ± 0.8	0.60 ± 0.46	0.86 ± 0.65
	150	200	15.0 ± 1.3	41 ± 5.1	0.76 ± 0.48	1.5 ± 0.46	2.1 ± 0.66
	150	300	30.2 ± 4.1	240 ± 21	0.069 ± 0.067	1.1 ± 0.53	1.6 ± 0.76
	250	300	21.5 ± 4.6	190 ± 21	0.41 ± 0.24	2.4 ± 0.67	3.3 ± 0.96
FF_d-IO	150	100	8.7 ± 0.9	3.1 ± 0.36	4.4 ± 3.2	1.8 ± 0.65	2.4 ± 0.86
	150	200	11.3 ± 0.6	16 ± 1.4	4.6 ± 1.6	4.1 ± 0.69	5.5 ± 0.91
	150	300	17.5 ± 0.7	79 ± 4.9	1.6 ± 0.46	5.5 ± 0.75	7.3 ± 1
	250	300	12.8 ± 0.5	35 ± 2.8	4.7 ± 1.4	6.2 ± 0.86	8.3 ± 1.2
FF_d-IF	150	100	7.5 ± 1.9	2.1 ± 0.18	2.6 ± 4.0	0.64 ± 0.49	0.91 ± 0.70
	150	200	9.5 ± 0.8	11 ± 0.87	3.3 ± 2.1	1.7 ± 0.53	2.4 ± 0.76
	150	300	10.5 ± 0.5	30 ± 2.4	4.9 ± 1.7	3.3 ± 0.56	4.7 ± 0.79
	250	300	8.5 ± 0.5	15 ± 1.1	8.3 ± 3.5	3.0 ± 0.63	4.3 ± 0.89

we provide laser-based particle data for the location in the flame corresponding to the maximum particle diameter, and for the sixth (FF_d-IF) we use the location of maximum Q_{vv} (this was necessary because the transmissivity at the point of maximum diameter was so close to unity that the uncertainty was unacceptably large). In general, the shape of the particle diameter curve (not shown) mimics the scattering curve, while the shapes of the laser extinction coefficient and volume fraction curves (not shown) look similar to the transmissivity curve.

To convert the scattering and extinction data into particle size and number density, the composition of the particles must be known. Here, analysis of numerical modeling results [3, 34] can provide insight. The calculations show that decomposition of $Fe(CO)_5$ leads to gas-phase Fe. If X_{in} is high enough and the temperature is low enough, the Fe will be a supersaturated vapor, and nucleation and growth of Fe particles may occur. However, a portion of the Fe may first react with O_2 to form FeO_2 that can react with O to form FeO. These iron oxides can also exist in a supersaturated vapor, and condense to give particles. If condensation and formation of iron oxides occur simultaneously, there may be some co-mingling of the compounds, or formation of particles with a core of one material and a shell of another. Although the uncertainty about particle material affects the data reduction, the exact material of the

TABLE 4

Effect of the Refractive Index on Particle Properties in FO-IO Flame with X_{in} = 300 ppm

Assumed particle composition	Scattering location	Mean diameter (nm)	Number density (cm^{-3})	Volume fraction
FeO	Air	8.7	7.5E + 10	4.1E-08
Fe	Air	6.0	2.4E + 11	4.4E-08
Fe_2O_3	Air	10.4	6.4E + 10	6.0E-08
FeO	Fuel	11.0	3.9E + 10	4.3E-08
Fe	Fuel	7.6	1.2E + 11	4.6E-08
Fe_2O_3	Fuel	13.1	3.3E + 10	6.2E-08

particles is unimportant in terms of removing inhibiting species, because there is a fixed amount of iron in the flame, and condensation of iron or its oxides both remove inhibiting species from the gas-phase. For addition of inhibitor to the fuel, the situation is somewhat clearer, as numerical calculations [34] show that almost all of the Fe is converted to FeO_2 without further conversion to FeO. Since data on the refractive index of FeO_2 are unavailable, we use FeO properties in the calculations. For air-side addition of $Fe(CO)_5$, we also use FeO properties in the calculations because data for FeOH, FeO_2, and $Fe(OH)_2$ are not available. Although these uncertainties in the condensation process make accurate and detailed analyses difficult, we present our limited results to provide a first estimate of the particle sizes, number densities and volume fractions in the flame zone.

Table 3 contains the results of scattering and extinction measurements for the FO-IO configuration (as well as the others). As the $Fe(CO)_5$ concentration increases, the mean diameter, extinction coefficient and volume fraction of the particles increase roughly linearly. The number density remains roughly constant, which implies that the formation of new particles from nucleation is balanced by changes in the total number density caused by coagulation. The mean diameter is on the order of 10 nm (typical soot primary particle size range is 10 nm to 40 nm [51]). The mean diameter may be smaller in the air-side peak than in the fuel-side peak, but the edge effects described above make comparisons tenuous. An increase in strain rate a from 150 s^{-1} to 250 s^{-1} results in a decrease in mean diameter, Q_{vv}, extinction coefficient, particle number density and volume fraction. The lower number density at a = 250 s^{-1} hints that small particles are merging together to form larger particles, but we do not have enough data to fully determine the particle nucleation and growth mechanisms.

Because the composition of the particles is estimated, it is worthwhile to calculate the sensitivity of results to the refractive index. For an FO-IO flame with X_{in} = 300 ppm, particle properties were calculated using three different particle compositions: Fe, FeO, and Fe_2O_3. The results (Table 4) show that relative to FeO, refractive index has an effect which is moderate for mean diameter (−30% for Fe and +20% for Fe_2O_3), large for number density (+218% and −15%), and moderate for volume fraction (+7% and +46%). (In previous work on iron-soot particles [52], a qualitatively similar dependence was found.) Although the refractive index has a significant effect on individual values, it does not affect the trends in the data for particles with constant composition. Nonetheless, if the particle composition changes while passing through the flame, the resulting change in refractive index could influence interpretation of the experimental results.

The scattering cross-section data show larger or more numerous particles when the inhibitor is added to the fuel (Fig. 8), rather than the air (Fig. 5). The data for FO-IF in Table 3 show the same behavior at lower strain rates. As X_{in} increases from 100 ppm to 300 ppm, the mean particle diameter doubles from 18 nm to 34 nm, which is two or three times larger than that of the FO-IO flames. The number density decreases with added $Fe(CO)_5$, which again may suggest that particles are merging to form larger

particles. The extinction coefficient and volume fraction remain roughly constant as $Fe(CO)_5$ concentration increases from 100 ppm to 300 ppm, but the experimental uncertainty is high, limiting the extent of the interpretation.

FO_d-IO Flames

Table 3 shows results for the FO_d-IO condition at three values of X_{in} at a = 150 s^{-1} and two values of strain at X_{in} = 300 ppm. The results are similar to those of the FO-IO condition for many properties: as X_{in} increases, the mean particle diameter, extinction co-efficient, and volume fraction increase in a linear fashion, while the number density remains constant (within experimental uncertainty). The mean particle diameter is again on the order of 10 nm, and an increase in the strain rate results in a decrease in the mean diameter. Unlike the FO-IO flame, however, an increase in the strain rate leads to an increase in the number density.

For the diluted-fuel flame (FO_d), the trends in the particle properties for fuel-side inhibitor addition (FO_d-IF) are similar to oxidizer-side addition (FO_d-IO), as presented in Table 3. Behavior of the number density, however, is markedly different for fuel side addition, for which it decreases by a factor of nearly 20 as X_{in} increases from 100 ppm to 300 ppm. This dramatic decrease may occur from surface growth and coalescence of smaller particles to form larger particles. Also, peak particle diameter for fuel-side addition is 1.3 to 3.0 times that for air-side addition. Compared to the FO-IF condition, which also has a large peak Q_{vv} on the fuel side of the stagnation plane, the measured particle diameter of the diluted-fuel flames with inhibitor added to the fuel stream (FO_d–IF) is 50% smaller at 100 ppm and 200 ppm, and nearly the same diameter at 300 ppm. A combination of shorter residence time and higher gas temperature is the cause of this difference, but there is not enough data to determine the relative importance of each cause.

FF_d-IO Flames

Table 3 shows results at the point of maximum diameter for the FF_d-IO condition at three values of X_{in} and two values of strain with X_{in} = 300 ppm. As X_{in} increases, the mean particle diameter, extinction coefficient, and volume fraction increase linearly, while the number density decreases. The mean particle diameter is on the order of 10 nm, which is similar to the other cases with inhibitor added to the oxidizer.

In the FF_d-IF condition, the point of maximum particle diameter occurs at a location of very high transmissivity (>99.5% at each X_{in}), which leads to excessively high uncertainty. In most cases, the uncertainty is higher than the measured value. As an alternative, we use the data from the point of peak scattering, which is an additional 0.4 mm toward the fuel stream, and has a transmissivity that is far enough from unity (98.5%–99.5%) to be measured with reasonable accuracy. Table 3 shows the measurements of particle properties for the three values of X_{in} and two strain rates at X_{in} = 300 ppm. Like the other flames with inhibitor in the fuel, the extinction coefficient and volume fraction increase with increasing X_{in}. The number density, however, increases with X_{in}, whereas in the other IF cases it decreases significantly. Similarly, the mean diameter increases only slightly with X_{in}, whereas for the other IF cases, the diameter doubles or triples. Hence, with the flame on the fuel side, increasing fuel-side inhibitor addition does not lead to the strong trend of coalescence. Rather, there is a mild increase in both diameter and number density.

CONCLUSIONS

Particle formation in counterflow diffusion flames of CH_4-N_2-O_2 inhibited by $Fe(CO)_5$ has been studied. Three counterflow diffusion flame configurations were investigated, with the flame on the fuel or oxidizer side of the stagnation plane, and inhibitor added to the fuel or the oxidizer stream. Numerically calculated Rayleigh cross sections agree well with the experimentally measured values for uninhibited flames, and support the use of calculated flame structures for assisting in interpretation of the experimental data. Laser-based particle size measurements in low strain rate flames show that the particles have diameters between 10 nm and 30 nm, number densities of 10^8 cm^{-3} to 10^{10} cm^{-3}, and volume fractions of 10^{-7} to 10^{-8}. Thermophoretic sampling and transmission

electron microscopy showed the particles to have primary particle diameters of 5 nm to 25 nm, with only slight agglomeration.

The particle scattering measurements in the counterflow diffusion flames suggest that particle formation reduces the inhibition effect of $Fe(CO)_5$, and that the time-temperature history of the particles has a large effect on their formation rate (and hence the inhibitor's loss of effectiveness), as opposed to the peak flame temperature. The time-temperature history of the nascent particles is most dependent upon the location of the flame (i.e., the peak temperature) relative to location of agent addition and the flow stagnation plane. Thermophoresis can also have a large effect on the particle velocity. The measurements are consistent with the hypothesis that the iron-containing intermediate species (which are believed to enter into the radical recombination reactions) are lost to a condensed phase, and become unavailable to interact with the radicals in regions where they affect the overall reaction rate. This may occur either through direct loss to the condensed phase where the peak radical mole fractions occur, or through particle formation upstream and subsequent convection of the particles away from the location of high radical mole fraction (which could occur because of 2-D thermophoresis). The present paper primarily measured particle scattering and inferred the effect on flame inhibition. To more clearly elucidate the influence of particle formation on flame inhibition, it would be of interest in future work to measure gas-phase iron-species concentrations, particle composition, and particle scattering off-axis, and model the particle growth process.

The present measurements in these laboratory flames have implications for both fire suppression and flame particle synthesis. For fire suppression, it is important for gas-phase chemical inhibitors to stay in the gas-phase. If conditions permit loss of the inhibiting species to a condensed phase and their subsequent convection away from regions of radical chain branching, the inhibitor may be much less effective. It may be advantageous to use low, non-condensing mole fractions of multiple inhibitors.

For particle synthesis, it may be important to control the flame location and temperature field (changeable through reactant dilution), the gas velocity, and the location of precursor addition to optimize the desired residence time in the appropriate chemical environment. For example, the proximity of the peak temperature to the stagnation plane can drastically affect the residence time in the low, moderate, and high temperature regions of the flames, through both convection or thermophoresis.

The authors thank undergraduate student intern Nikki Prive for assistance with data acquisition and uncertainty analysis programs and Maria Aquino for operating the electron microscope and advising us on sampling techniques. Discussions with Dr. George Mulholland about particle measurement techniques and Dr. Quang-Viet Nguyen about beam steering contributed greatly to this work. This research is part of the Department of Defense's Next Generation Fire Suppression Technology Program, funded by the DoD Strategic Environmental Research and Development Program (SERDP).

REFERENCES

1. Lask, G., and Wagner, H. G., *Proc. Combust. Inst. Vol. 8* Williams and Wilkins Co., Baltimore, 1962, pp. 432–438.
2. Reinelt, D., and Linteris, G. T., *Proc. Combust. Inst.* 26:1421 (1996).
3. Rumminger, M. D., Reinelt, D., Babushok, V., and Linteris, G. T., *Combust. Flame* 116:207 (1999).
4. Linteris, G. T., Rumminger, M. D., Babushok, V. I., and Tsang, W., *Proc. Combust. Inst.* 28:2939 (2000).
5. Rumminger, M. D., and Linteris, G. T., *Combust. Flame* 120:451 (2000).
6. Rumminger, M. D., and Linteris, G. T., *Combust. Flame* 123:82 (2000).
7. Linteris, G. T., Rumminger, M. D., and Babushok, V. I., *Combust. Flame* 122:58 (2000).
8. Milne, T. A., Green, C. L., and Benson, D. K., *Combust. Flame* 15:255 (1970).
9. Hamins, A., Trees, D., Seshadri, K., and Chelliah, H. K., *Combust. Flame* 99:221 (1994).
10. Fallon, G. S., Chelliah, H. K., and Linteris, G. T., *Proc. Combust. Inst.* 26:1395 (1996).
11. Macdonald, M. A., Jayaweera, T. M., Fisher, E. M., and Gouldin, F. C., *Combust. Flame* 116:166 (1999).
12. Zegers, E. J. P., Williams, B. A., Fisher, E. M., Fleming, J. W., and Sheinson, R. S., *Combust. Flame* 121:471 (2000).
13. Simmons, R. F., and Wolfhard, H. G., *Trans. Faraday Soc.* 52:53 (1956).
14. Niioka, T., Mitani, T., and Takahashi, M., *Combust. Flame* 50:89 (1983).

15. Miller, E., and McMillion, L. G., *Combust. Flame* 89:37 (1992).
16. Masri, A. R., *Combust. Sci. Technol.* 96:189 (1994).
17. Masri, A. R., Dally, B. B., Barlow, R. S., and Carter, C. D., *Combust. Sci. Technol.* 114:17 (1996).
18. Trees, D., Grudno, A., and Seshadri, K., *Combust. Sci. Technol.* 124:311 (1997).
19. MacDonald, M. A., Jayaweera, T. M., Fisher, E. M., and Gouldin, F. C., *Proc. Combust. Inst.* 27:2749 (1998).
20. Wooldridge, M. S., *Prog. Energy Combust. Sci.* 24:63 (1998).
21. Puri, I. K., and Seshadri, K., *Combust. Flame* 65:137 (1986).
22. Seshadri, K., and Williams, F. A., *Int. J. Heat Mass Transfer* 21:137 (1978).
23. Rudder, R. R, and Bach, D. R., *J. Optical Society of America* 58:1260 (1968).
24. Landolt-Bornstein, *Numerical Data and Functional Relationships in Science and Technology*, Springer-Verlag, Berlin, 1993.
25. Hahn, D. W., Ph.D. Dissertation, Louisiana State University, 1992.
26. Granqvist, C. G., and Buhrman, R. A., *J. Appl. Phys.* 47:2200 (1976).
27. Xing, Y. C., Koylu, U. O., and Rosner, D. E., *Combust. Flame* 107:85 (1996).
28. Kasper, G., Shon, S. N., and Shaw, D. T., *Am. Ind. Hyg. Assoc. J.* 41:288 (1980).
29. Hahn, D. W., and Charalampopoulos, T. T., *Proc. Combust. Inst.* 24:1007 (1992).
30. Hinds, W. C., *Aerosol Technology; Properties, Behavior, and Measurement of Airborne Particles.* John Wiley & Sons, Inc., New York, 1982.
31. Mulholland, G., Personal Communication, Dec. 2000.
32. Taylor, B. N., and Kuyatt, C. E., *Guidelines for Evaluating and Expressing the Uncertainty of NIST Measurement Results* National Institute of Standards and Technology, NIST Technical Note 1297, 1994.
33. Moffat, R. J., *Transactions of the ASME* 104:250 (1982).
34. Rumminger, M. D., and Linteris, G. T., *Fire Safety Science: Proceedings of the Sixth International Symposium,* International Association for Fire Safety Science, Marne-La-Vallee, France, 2000, pp. 289–300.
35. Smooke, M. D., Puri, I. K., and Seshadri, K., *Proc. Combust. Inst.* 21:1783 (1986).
36. Kee, R. J., Rupley, F. M., and Miller, J. A., *CHEMKIN-II: A Fortran Chem. Kinetics Package for the Analysis of Gas Phase Chem. Kinetics* Sandia National Laboratory, SAND89–8009B, 1989.
37. Kee, R. J., Dixon-Lewis, G., Warnatz, J., Coltrin, R. E., and Miller, J. A., *A Fortran Computer Package for the Evaluation of Gas-Phase, Multicomponent Transport Properties* Sandia National Laboratory, SAND86–8246, 1986.
38. Peters, N., in *Reduced Kinetic Mechanisms for Applications in Combustion Systems* (Peters, N, and Rogg B., Eds.), Springer-Verlag, New York, pp. 3–14, 1993.
39. D'Alessio, A., in *Particulate Carbon. Formation during Combustion* (D. C. Siegla and G. W. Smith, Eds.), Plenum Press, New York, pp. 207–256;1981.
40. Skaggs, R. R., Daniel, R. G., Miziolek, A. W., McNesby, K. L., Babushok, V. I., Tsang, W., and Smooke, M. D., *Halon Options Technical Working Conference.* Albuquerque, N. M., 1999, pp. 117–131.
41. Zachariah, M. R., Chin, D., Semerjian, H. G., and Katz, J. L., *Combust. Flame* 78:287 (1989).
42. Chung, S. L., and Katz, J. L., *Combust. Flame* 61:271 (1985).
43. Hung, C. H., Miquel, P. F., and Katz, J. L., *J. Mater. Res.* 7:1870 (1992).
44. Miquel, P. F., and Katz, J. L., *J. Mater. Res* 9:746 (1994).
45. Andac, M. G., Egolfopoulos, F. N., Campbell, C. S., and Lauvergne, R., *Proc. Combust. Inst.* 28:2921 (2000).
46. Lentati, A. M, and Chelliah, H. K., *Combust. Flame* 115:158 (1998).
47. Gomez, A., and Rosner, D. E., *Combust. Sci. Technol.* 89:335 (1993).
48. Waldmann, L., and Schmidt, K. H., in *Aerosol Science* (C. N. Davies, Ed.), Academic Press, New York, pp. 137–162, 1966.
49. Talbot, L., Cheng, R. K., Schefer, R. W., and Willis, D. R., *J. Fluid Mech.* 101:737 (1980).
50. Weinberg, F. J., *Optics of Flames.* Butterworth, London, 1963
51. Megaridis, C. M., and Dobbins, R. A., *Combust. Sci. Technol.* 71:95 (1990).
52. Charalampopoulos, T. T., Hahn, D. W., and Chang, H., *Appl. Opt.* 31:6519 (1992).

Received 12 March 2001; revised 12 September 2001; accepted 1 October 2001